nature physics

Fast universal control of an oscillator with weak dispersive coupling to a qubit

Alec Eickbusch [1,2] ✉, Volodymyr Sivak[1,2], Andy Z. Ding[1,2], Salvatore S. Elder[1,2], Shantanu R. Jha [1,2], Jayameenakshi Venkatraman [1,2], Baptiste Royer[1,2], S. M. Girvin [1,2], Robert J. Schoelkopf[1,2] and Michel H. Devoret [1,2] ✉

Full manipulation of a quantum system requires controlled evolution generated by nonlinear interactions, which is coherent when the rate of nonlinearity is large compared with the rate of decoherence. As a result, engineered quantum systems typically rely on a bare nonlinearity much stronger than decoherence rates, and this hierarchy is usually assumed to be necessary. Here we challenge this assumption by demonstrating the universal control of a quantum system where the rate of bare nonlinear interaction is comparable to the fastest rate of decoherence. We introduce a noise-resilient protocol for the universal quantum control of a nearly harmonic oscillator that takes advantage of an in situ enhanced nonlinearity instead of harnessing a bare nonlinearity. Our experiment consists of a high-quality-factor microwave cavity with weak dispersive coupling to a superconducting qubit with much lower quality. By using strong drives to temporarily excite the oscillator, we realize an amplified three-wave-mixing interaction, achieving typical operation speeds over an order of magnitude faster than expected from the bare dispersive coupling. Our demonstrations include the preparation of a single-photon state with high fidelity, the generation of squeezed vacuum with large intracavity squeezing and measurement-free preparation of logical states for the binomial and Gottesman–Kitaev–Preskill quantum error-correcting codes.

A strong nonlinearity relative to decoherence is crucial for the coherent control of a quantum system[1]. Because of this, many quantum physics experiments strive to operate in a regime where the relevant rate of undriven nonlinear interaction is orders of magnitude larger than the fastest rate of decoherence. Such a hierarchy is at the heart of most engineered quantum systems, including the prototypical realizations of cavity quantum electrodynamics (QED) with Rydberg atoms[2], nonlinear quantum electromechanics[3], hybrid superconductor–semiconductor systems[4] and circuit QED[5]. With this prevalence, it is natural to question if a large native nonlinearity relative to decoherence is required for high-fidelity operations, or if a driven, enhanced nonlinearity could be used instead.

To address this question, here we introduce and demonstrate universal control compatible with the weak dispersive regime of circuit QED, arriving at the counterintuitive result that a large bare nonlinear interaction is not required for the coherent control of an oscillator. The technique could be adapted to many dispersive cavity-QED-like hybrid architectures such as those including superconducting qubits[5], acoustic modes[3,6,7], semiconducting qubits[4], electrons on helium[8] or Rydberg atoms[9]. Such a weak coupling approach can also be beneficial as a means to selectively control a single oscillator when multiple oscillators are coupled to the same qubit[10]. In our proof-of-principle demonstration, the oscillator is realized as the lowest-energy mode of a superconducting microwave cavity,

[1]Departments of Applied Physics and Physics, Yale University, New Haven, CT, USA. [2]Yale Quantum Institute, Yale University, New Haven, CT, USA. ✉e-mail: alec.eickbusch@yale.edu; michel.devoret@yale.edu

and the ancillary qubit is realized by the lowest two energy levels of a transmon.

Oscillators can be controlled by coupling to an ancillary qubit in the dispersive regime described by the Hamiltonian $H/\hbar = \chi a^\dagger a \sigma_z/2$, where a is the annihilation operator of the oscillator, σ_z is the Pauli-Z operator of the qubit and $\hbar$ is the reduced Planck constant. State-of-the-art universal control methods include the qubit cavity mapping protocol[11], the selective number-dependent arbitrary phase (SNAP) and displacement gate set[12–15], measurement-based methods for oscillator state preparation[16] or pulse-shaping methods such as gradient ascent pulse engineering (GRAPE)[17–19]. These methods can perform relevant operations in time comparable to $2\pi/\chi$, so the bare dispersive shift is usually engineered to be orders of magnitude larger than the fastest decoherence rate in the system, that is, $\chi/2\pi \gg \max(\Gamma_2, \Gamma_1, \kappa)$, where $\Gamma_2 = 1/T_2$ and $\Gamma_1 = 1/T_1$ are the qubit decoherence and relaxation rates, respectively, and κ is the oscillator relaxation rate[5,20].

Instead, to realize universal control in the weak dispersive regime where $\chi/2\pi \lesssim \max(\Gamma_2, \Gamma_1, \kappa)$, we use resonant microwave drives to induce phase-space displacements of the oscillator far from the origin. With this, the weak four-wave-mixing dispersive interaction is transformed into an effective three-wave-mixing interaction between the oscillator relative to its displaced centre of mass and the qubit. A similar scheme is used for enhancing the mixing processes in quantum parametric amplification[21] and optomechanical coupling[22]; however, in these applications, the resulting lower-order interactions around the centre of mass are linear and thus not universal. In addition, some circuit QED experiments have harnessed driven four-wave mixing to generate enhanced three-wave-mixing interactions between an oscillator and qubit at rates faster than the native dispersive shift[19,23–31]; however, high-fidelity universal control faster than $2\pi/\chi$ has not been previously demonstrated, to the best of our knowledge.

The phase-space displacement acts as a lever arm under the dynamics of dispersive interaction (Fig. 1a). To analyse this effect, H can be transformed into a displaced frame, giving

$$\tilde{H}/\hbar = \chi a^\dagger a \frac{\sigma_z}{2} + \chi(\alpha(t)a^\dagger + \alpha^*(t)a)\frac{\sigma_z}{2} + \chi|\alpha(t)|^2 \frac{\sigma_z}{2}, \qquad (1)$$

where $\partial_t \alpha(t) = -i\varepsilon(t) - (\kappa/2)\alpha(t)$ is the classical response to a resonant drive, namely, $H_d/\hbar = \varepsilon^*(t)a + \varepsilon(t)a^\dagger$. With a large displacement $\alpha_0 = \max|\alpha(t)|$, the second term in $\tilde{H}$ dominates, and the effective interaction between the oscillator and qubit becomes a qubit-state-dependent force with the maximum effective interaction strength $g_{\text{eff}} = \chi\alpha_0$ (refs. [23,25,29]). For a transmon with anharmonicity K, the critical oscillator photon number limits the enhanced interaction to $g_{\text{eff}}^{\max} \approx \sqrt{\chi K/6}$ (Methods).

Large displacements populate highly excited states of the oscillator, enhancing some decoherence mechanisms. Fortunately, there is no additional decoherence caused by oscillator photon loss after a coherent displacement provided the deterministic re-centring force at a rate $\kappa/2$ is included when calculating the drive $\varepsilon(t)$ needed for the desired displacement trajectory $\alpha(t)$. However, oscillator dephasing at a rate κ_ϕ causes enhanced decoherence under a displacement, resulting in diffusion-like terms at an effective rate $2|\alpha(t)|^2\kappa_\phi$ (Methods). Oscillators such as superconducting cavities can have dephasing rates much weaker than their relaxation rates limiting this effect[27,29,32]; however, it reveals a trade-off between faster control with large displacements and enhanced loss from oscillator dephasing (Supplementary Section 6).

With this in mind, the enhanced three-wave-mixing interaction and a qubit π-pulse can be used to engineer an entangling gate dubbed the echoed conditional displacement (ECD) gate, defined as $\text{ECD}(\beta) = D(\beta/2)|e\rangle\langle g| + D(-\beta/2)|g\rangle\langle e|$, where $D(\alpha) = e^{\alpha a^\dagger - \alpha^* a}$ is the displacement operator and $\{|g\rangle, \langle e|\}$ are the ground and excited states of the qubit, respectively. A version of the gate was first implemented as a tool to realize the error correction of the Gottesman–Kitaev–Preskill (GKP) qubit manifold of states[29]. With an intermediate oscillator
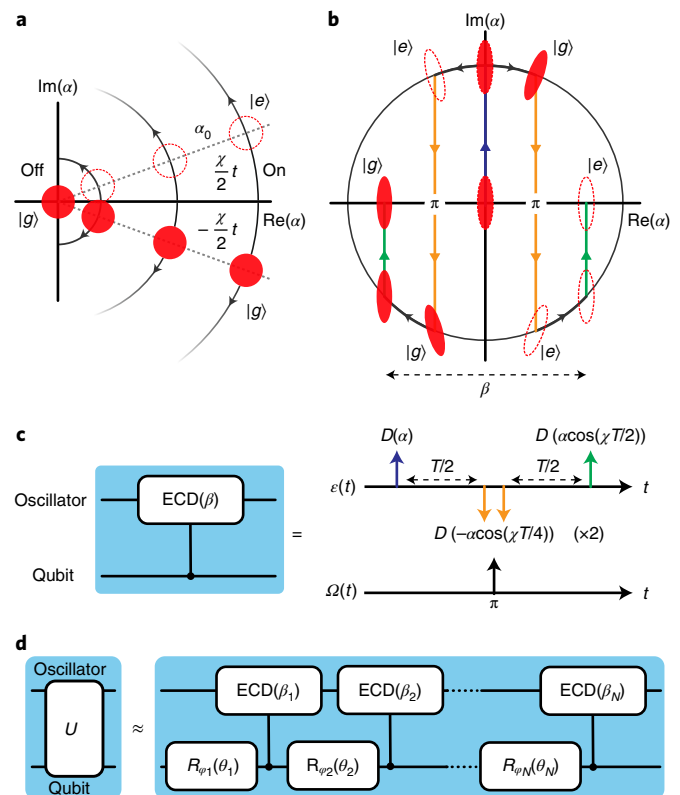

Fig. 1 | ECD control. a, Under conditional rotation, phase-space displacements act as lever arms, generating a large separation conditioned on the qubit states $|g\rangle$ and $|e\rangle$. Here three displacements are shown acting on vacuum; with larger α_0, there is a larger state separation after time t. **b**, ECD-gate phase-space trajectory in the limit of instantaneous displacements acting on a squeezed state for illustration. **c**, Oscillator drive ($\varepsilon(t)$) and qubit drive ($\Omega(t)$) for the ideal ECD gate of duration T resulting in a final-state separation of $\beta = 2i\alpha\sin(\chi T/2)$, where $|\alpha| = \alpha_0$. **d**, Any unitary can be approximated by a sequence of N single-qubit rotations and ECD gates with a built-in dynamical decoupling generated through the symmetric construction of the full sequence.

displacement of length α_0, the $\text{ECD}(\beta)$ gate occurs in a time of approximately $|\beta|/(\chi\alpha_0)$ through the trajectory (Fig. 1b) and ideal drive sequence (Fig. 1c). The ECD gate cancels the dynamics from the dispersive and Stark-shift terms in $\tilde{H}$ up to a qubit phase because of its symmetric construction and qubit echo (Supplementary Section 4).

To build a full gate set, we combine the $\text{ECD}(\beta)$ gate with unselective qubit rotations, $R_\varphi(\theta) = \exp(-i(\theta/2)(\sigma_x\cos\varphi + \sigma_y\sin\varphi))$. The rotation pulse bandwidth must be sufficiently large compared with $\langle a^\dagger a\rangle\chi$ so that the oscillator state does not entangle with the qubit during rotations. As a result, a large transmon anharmonicity satisfying $K \gg \chi$ is needed to avoid populating higher-excited states of the transmon. Together, the set $\{\text{ECD}(\beta), R_\varphi(\theta)\}$ is universal for the control of oscillator and qubit (Methods). Any desired unitary on the joint oscillator and qubit Hilbert space is approximated by the decomposition shown in Fig. 1d, with four real-valued parameters per step, and a fidelity that depends on circuit depth N. The full sequence has a total duration of $T_{\text{total}} = (\chi\alpha_0)^{-1}\sum_{i=1}^{N}|\beta_i|$ in the instantaneous displacement and qubit pulse limit; hence, a large $\alpha_0 \gg 1$ can enhance the overall speed of a target unitary. Every ECD control sequence has an intrinsic dynamical decoupling of low-frequency noise coupled to σ_z because of its designed symmetric structure, motivating the choice of this gate set.

To realize a desired unitary or state transfer with the ECD gate set, we use a two-step optimization approach. In the first step, we find the circuit parameters $\{\vec{\beta}, \vec{\varphi}, \vec{\theta}\}$ that maximize the fidelity and minimize the circuit depth N. Here we use an efficient gradient-based parameter optimization using automatic differentiation implemented on a
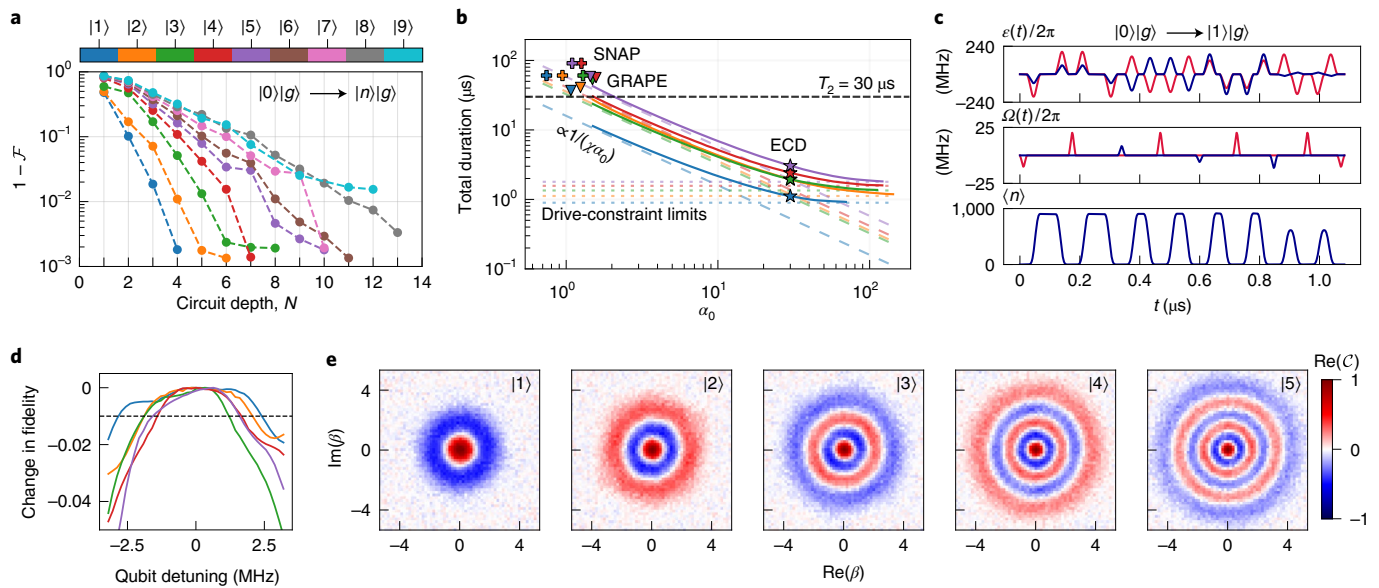
Fig. 2 | Fock state preparation. a, Best state-transfer infidelity found when optimizing the ECD circuit parameters to prepare oscillator Fock state $|n\rangle$ from vacuum as a function of circuit depth N. Here $\mathcal{F} = |\langle g| \langle n| U_{ECD} |0\rangle |g\rangle|^2$. **b**, Total pulse-sequence duration using the protocols from **a** with minimum N such that $\mathcal{F} \geq 0.99$ (solid lines). The colour code is the same as **a**. The coloured long-dashed lines are the instantaneous displacement scaling $T_{total} = (\chi\alpha_0)^{-1} \sum_{i=1}^{N} |\beta_i|$. The coloured dotted lines are the drive-constraint limits $T_{total} = 2Nt_q + 4Nt_D$. We use $\alpha_0 = 30$ in our experiment, as indicated by the stars. Durations for independently optimized GRAPE (triangles) and SNAP (crosses) protocols are also included using our system parameters, where the x coordinate indicates the simulated largest displacement used ($\max|\langle a\rangle|$). **c**, Cavity drive $\varepsilon(t)$ (top) and transmon drive $\Omega(t)$ (middle) for the preparation of Fock state $|1\rangle$ (real and imaginary parts shown in red and blue, respectively) and simulated average photon number during the sequence (bottom). **d**, Simulated drop in fidelity of the Fock-state preparation sequences with qubit detuning $H/\hbar = \delta_z\sigma_z/2$. The dashed line indicates a drop of 1%. **e**, Measured real part of the characteristic functions for the first five excited Fock states in the cavity. The preparation fidelities are given in Table 1.

graphics processing unit. A batch of 500 circuits are randomly initialized and optimized in parallel to realize multistart optimization (Supplementary Section 7).

As an example of this first step of optimization, we focus on the preparation of Fock states in the oscillator, namely, $|0\rangle|g\rangle \rightarrow |n\rangle|g\rangle$. These are not simple superpositions of displaced coherent states; therefore, it is not obvious that they can be easily prepared using conditional displacements starting from vacuum. Optimization results for the preparation of Fock states $|1\rangle$–$|9\rangle$ are shown in Fig. 2a. The required circuit depth increases with the photon number, with ten or fewer ECD gates needed to reach a state-transfer fidelity $\mathcal{F} > 0.99$ for the first seven Fock states. This example shows that ECD control can be an efficient circuit parameterization, with only $4N$ total parameters per sequence, a circuit depth comparable to the SNAP protocol[12,14,15], and over an order of magnitude fewer parameters than time-domain GRAPE as used in state-of-the-art bosonic experiments[20].

In the second optimization step, the cavity drive $\varepsilon(t)$ and qubit drive $H_q/\hbar = \Omega^*(t)\sigma^- + \Omega(t)\sigma^+$ are compiled from a set of ECD circuit parameters found in the first step. This optimization is done with realistic constraints to realize the ECD sequence in the shortest time given the bandwidth and amplitude limits (Supplementary Sections 3 and 4).

In our experiment, we use a three-dimensional aluminium superconducting cavity (frequency, 5.26 GHz; relaxation time, $T_{1,c} = 436$ μs) coupled to a transmon qubit (frequency, 6.65 GHz; relaxation time, $T_{1,q} \approx 50$ μs; anharmonicity $K/2\pi = 193$ MHz) with a dispersive shift $\chi/2\pi = 33$ kHz. Given this bare nonlinearity, the resulting sequence duration for the preparation of Fock states $|1\rangle$–$|5\rangle$ as a function of displacement used during the ECD gates α_0 is shown in Fig. 2b. We use the circuits with the shortest depth such that the optimized fidelity (Fig. 2a) is greater than 99%. This choice represents an optimum fidelity in the presence of decoherence as verified by the master equation simulations. At intermediate values of α_0, the sequence duration follows the instantaneous displacement limit $T_{total} \propto (\chi\alpha_0)^{-1}$. As α_0 increases, the amplitude and bandwidth constraints result in sequences limited by the total duration

of the constituent pulses, that is, $T_{total} = 2Nt_q + 4Nt_D$, where the duration of qubit rotation pulse and oscillator displacement pulses used in our experiment are $t_q = 24$ ns and $t_D = 44$ ns, respectively (Supplementary Section 4). In our experimental demonstrations, we use $\alpha_0 = 30$ (Fig. 2b, stars) and operate close to the predicted maximum conditional displacement rate $g_{eff}^{max}/2\pi \approx 1$ MHz. The shortest lifetime in our experiment is the transmon Ramsey coherence time $T_2 \approx 30$ μs realizing $\chi/2\pi \lesssim \Gamma_2 \ll g_{eff}/2\pi$ and allowing high-fidelity control in a regime where bare nonlinearity is comparable to the fastest decoherence rate.

In Fig. 2b, the duration of ECD pulse sequences are also compared with independently optimized GRAPE and SNAP sequences for Fock state preparation with our system parameters (Supplementary Section 9). Here ECD sequences have over an order of magnitude enhancement in gate speed. For example, single-photon state preparation in the oscillator is realized about 30 times faster than $2\pi/\chi$, with compiled drives and simulated intracavity average photon number shown in Fig. 2c. This demonstrates the ability to utilize the oscillator's vast Hilbert space to enhance the gate speed with a displaced field of $\max|\alpha|^2 = 900$ photons during the gates. To indicate the insensitivity to low-frequency σ_z noise, Fig. 2d shows the simulation results for ECD Fock-state-preparation pulse sequences with an additional qubit detuning $H/\hbar = \delta_z\sigma_z/2$, showing resilience at the level of $1 - \mathcal{F} \approx 0.01$ to static detuning on the order of $\delta_z/\hbar \approx 1$ MHz.

In the experiment, we measure the complex-valued characteristic function $\mathcal{C}(\beta) = \text{Tr}(D(\beta)\rho)$ by using an ECD gate to perform phase estimation of the displacement operator $D(\beta)$ conditioned on a disentangling transmon measurement (Supplementary Section 5)[29,33,34]. Importantly, tomography can also be performed in a time much faster than $2\pi/\chi$ using large displacements (note that direct Wigner tomography using typical circuit-QED parity measurements would be impractical, taking a time of $\pi/\chi \approx 15$ μs). The real parts of the measured characteristic functions for Fock states $|1\rangle$–$|5\rangle$ are shown in Fig. 2e. From the real and imaginary parts (not shown) of the characteristic functions, we reconstruct the density matrices using maximum

Table 1 | Measured and simulated state preparation fidelities

State	$\mathcal{F}_{exp}$ (%)	$\mathcal{F}_{sim}$ (%)	$\mathcal{F}_{sim}^{\kappa_\phi}$ (%)
$|1\rangle$	98	99	98
$|2\rangle$	92	97	94
$|3\rangle$	88	97	93
$|4\rangle$	87	97	92
$|5\rangle$	82	94	83
$|+Z\rangle_{bin}$	92	98	95
$|+X\rangle_{bin}$	89	97	94
$|+Y\rangle_{bin}$	91	97	93
$|+Z\rangle_{GKP}$	85	93	85
$|+Y\rangle_{GKP}$	83	92	87
$|-Z\rangle_{GKP}$	80	93	85

$\mathcal{F}_{exp}$ is the measured fidelity found from density matrix reconstruction, $\mathcal{F}_{sim}$ is the simulated fidelity including all the independently measured decoherence rates and $\mathcal{F}_{sim}^{\kappa_\phi}$ is the simulated fidelity including additional cavity dephasing at rate $\kappa_\phi = (150\,\text{ms})^{-1}$. Fidelity is defined as $\mathcal{F} = \langle\psi_t| \rho_g |\psi_t\rangle$, where ρ_g is the oscillator state after projecting the qubit in $|g\rangle$ and $|\psi_t\rangle$ is the oscillator target state. We estimate that the quoted fidelities are accurate within 1% using bootstrapping. The average probability of measuring $|g\rangle$ after the state preparation sequences are {0.96, 0.93, 0.96, 0.92} for the Fock, squeezed, binomial and GKP states, respectively.

likelihood estimation leading to the results summarized in Table 1 and reaching the best fidelity of $\mathcal{F}_{exp} = 0.98 \pm 0.01$ for Fock state $|1\rangle$.

The experimental fidelities listed in Table 1 are compared with master equation simulations $\mathcal{F}_{sim}$ including all the independently measured decoherence mechanisms (Supplementary Section 6). Out of the measured decoherence sources, qubit relaxation during the ECD gates is the largest error contribution. The simulated fidelities are higher than the measured fidelity for most demonstrations, and a likely cause is the additional coherent error sources arising from unknown microwave transfer functions, calibration drifts and other forms of model bias. Closed-loop optimization strategies such as reinforcement learning could be used to mitigate these effects[35,36], but in this work, we did not perform such an optimization. An additional possible decoherence mechanism is pure oscillator dephasing that could arise from coupling to other uncontrolled modes such as two-level systems[37]. Although we do not have an exact measurement of the pure oscillator dephasing rate in this experiment, we have simulated the influence of relatively slow pure oscillator dephasing at a rate $\kappa_\phi = (150\,\text{ms})^{-1}$, resulting in sequences with fidelities given by $\mathcal{F}_{sim}^{\kappa_\phi}$ (Table 1). These results reveal that even a small pure dephasing rate of the oscillator can substantially lower the fidelity when using large displacements.

As a second demonstration, we prepare squeezed vacuum states $|\zeta\rangle = \exp\left((\zeta^* a^2 - \zeta a^{\dagger 2})/2\right)|0\rangle$ with a squeezing level in decibels defined as $20\log_{10}(e^{|\zeta|})$. Highly squeezed states of an oscillator can allow sensing beyond the standard quantum limit, as was recently used to enhance the search for dark matter axions[38]. However, the presence of a large oscillator self-Kerr degrades the quality by distorting the squeezed state and increasing the variance of squeezed quadrature[39]. In our experiment, the small inherited oscillator self-Kerr of ~1 Hz, over three orders of magnitude smaller than is typically used[18], minimizes the state distortion during preparation and idling periods.

In Fig. 3a (left), we show the ECD optimization results for squeezed state preparation starting from vacuum. We plot the minimum circuit depth needed to reach fidelity $\mathcal{F} \geq 99\%$. A related method for squeezed state creation was introduced elsewhere[40], and the protocols here have fewer conditional displacements, demonstrating the ability of our optimization method to find novel control circuits. In our experiment, we apply the optimized squeezed-state-preparation ECD sequences for target squeezing levels of {6, 8, 10, 12, 14} dB using $\alpha_0 = 30$. The measured characteristic functions are shown in Fig. 3b, with achieved squeezing levels of {4.8, 6.7, 8.2, 9.8, 11.1} dB calculated from a fit to the reconstructed probability distribution along the squeezed quadrature

(Supplementary Section 5). The reconstructed states show some non-Gaussian features as decoherence during the pulse causes distortion, similar to the Fock preparation case, leading to a lower effective squeezing. To the best of our knowledge, the measured squeezing of 11.1 dB demonstrated here is larger than any intraresonator squeezing demonstration in the microwave regime to date, with other demonstrations achieving steady-state intracavity squeezing at the level of 8.2 dB (ref. [39]) and a post-selected state preparation method demonstrating 5.7 dB (ref. [16]). The ECDs realized here could also be used to sense small displacements of a squeezed state using phase estimation[41].

To further characterize the method, we implement logical state preparation for two different quantum error-correcting bosonic codes: the binomial code[42] and the square GKP code[43]. For the binomial code, we focus on the smallest code for which the loss of a single photon is correctable, with code words $|+Z\rangle_{bin} = (|0\rangle + |4\rangle)/\sqrt{2}$ and $|-Z\rangle_{bin} = |2\rangle$. The GKP code, on the other hand, is defined as the mutual +1 eigenspace of the displacement stabilizers $S_p = D(\sqrt{2\pi})$ and $S_q = D(i\sqrt{2\pi})$ with logical operators given by $X = D(\sqrt{\pi/2})$ and $Z = D(i\sqrt{\pi/2})$. The ideal GKP code has infinite energy, and a finite-energy code can be defined by modifying the stabilizers and logical operators using the envelope operator $E_\delta = \exp\{-\delta^2 a^\dagger a\}$ under the transformation $O_\delta = E_\delta O E_\delta^{-1}$, leading to code states that are superpositions of squeezed states with squeezing parameter $\zeta = \ln\delta$ (refs. [44,45]).

For the binomial code, previous experiments have demonstrated logical state preparation using GRAPE, relying on a large bare nonlinearity $\chi/2\pi$ compared with decoherence rates[18,46–49]. With ECD control, the optimization results in protocols that prepare all the cardinal points of the Bloch sphere to a fidelity of $\mathcal{F} = 99\%$ with a circuit depth at most $N = 5$. Applying these circuits in experiment using $\alpha_0 = 30$ results in the measured characteristic functions shown in Fig. 3c with fidelity given in Table 1. The average pulse time for binomial state preparation is 3.27 μs—about nine times faster than $2\pi/\chi$. In principle, fast logical operations, measurement and stabilization of the binomial code could also be performed using ECD control.

For GKP states, Fig. 3a (right) shows the circuit depth required for ECD protocols to prepare $|+Z\rangle_{GKP}$, $|+Y\rangle_{GKP}$ and $|-Z\rangle_{GKP}$ optimized to a state-transfer fidelity of $\mathcal{F} = 98\%$ at different squeezing levels. The protocols found here represent a unitary protocol for GKP state creation, as opposed to the non-unitary protocols recently demonstrated in both trapped ions[34] and superconducting circuits[29] that require multiple measurements with feedback or many rounds of dissipative pumping. A related protocol for measurement-free GKP state preparation has been proposed[50] and implemented in trapped ions[51]; however, it requires an initial squeezed state.

In Fig. 3d, we plot the measured characteristic functions found using these circuits with $\alpha_0 = 30$, achieving fidelities given in Table 1. For the GKP states, we use a target squeezing level of 10.3 dB and experimentally achieve a squeezing level of 9.1 dB (Supplementary Section 5). Our pulse sequences are about 15 times faster than the state preparation method using measurements and feedback demonstrated in another work[29] with similar experimental parameters. This order of magnitude reduction in initialization time can reduce the hardware overhead of error correction protocols requiring GKP resource states, such as teleported error correction[52] or GKP surface code[53,54].

The experimental demonstrations in this work have focused on oscillator state preparation; however, the ECD protocol is universal and can also be extended to performing fast unitary gates. As a demonstration of this, in Supplementary Section 8, we show the numerical optimization of the logical $S = \text{diag}(1, e^{i\pi/2})$ and $T = \sqrt{S} = \text{diag}(1, e^{i\pi/4})$ gates for a finite-energy GKP code at different squeezings δ. Remarkably, a circuit depth of only $N = 3$ is required to reach a gate fidelity of $\overline{\mathcal{F}} \approx 0.99$ for the T gate and $N = 4$ for the S gate at $\delta = 0.25$, revealing that the ECD gate set is well suited for control over the finite-energy GKP code.

With these proof-of-principle results, we demonstrate the counterintuitive result that high-fidelity universal control can be carried
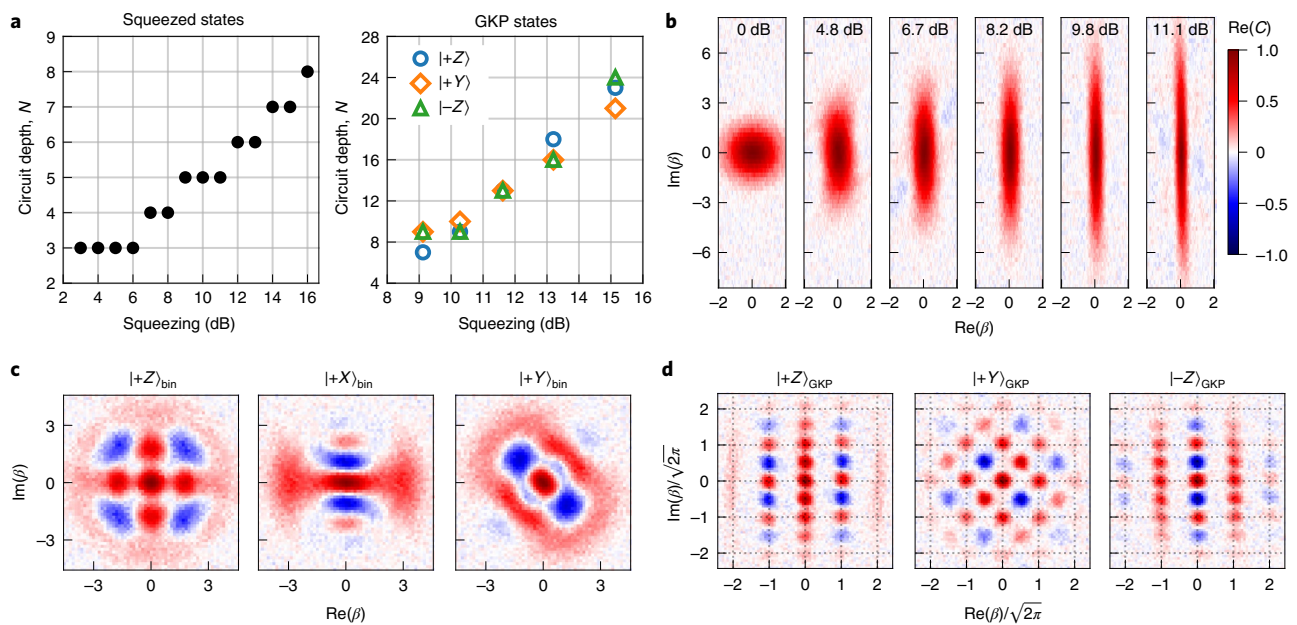
Fig. 3 | Preparation of squeezed states and bosonic code words. a, Numerically optimized minimum circuit depth to reach state-transfer fidelity $\mathcal{F} \geq 0.99$ for the preparation of squeezed states (left) and $\mathcal{F} \geq 0.98$ for preparation of logical GKP states (right). **b**, Real part of the measured characteristic functions for vacuum and squeezed states, with the achieved squeezing indicated.

c,d, Measured characteristic functions for logical state preparation of binomial (**c**) and GKP (**d**) code words. For the binomial code, $|-Z_L\rangle = |2\rangle$ is included in Fig. 2e. For both codes, all the other cardinal points on the Bloch sphere can be obtained by phase-space rotations. Fidelities for the binomial and GKP code are given in Table 1, with an additional analysis given in Supplementary Section 5.

out in a regime where the relevant rate of bare nonlinear evolution is comparable to the fastest decoherence rate. In particular, a large on–off ratio between the rate of control and bare oscillator–qubit hybridization can be achieved without the need for additional hardware such as a tunable coupler. Importantly, the approach still requires a large ancilla qubit nonlinearity K, reflected by the enhanced interaction speed limit directly proportional to $\sqrt{\chi K}$.

Although our examples are specific to the oscillator and qubit system, similar displaced-field-type control schemes could be designed and performed in other bosonic systems with bare nonlinearity of the fourth order or greater, such as the recently proposed scheme to enhance the rate of Fock state preparation in a Kerr oscillator[55]. The construction shown in Fig. 1d and parameter optimizations shown in this work could also be applied to realize the universal control of the motional state of a trapped ion. In such systems, spin-dependent forces can be used to realize conditional displacement[56], and circuits similar to those presented here have been demonstrated for application-specific control[34,51].

Finally, weak bare nonlinearity has many benefits in the context of quantum information processing—for example, by sufficiently reducing dispersive coupling χ, oscillator nonlinearity and loss inherited from the qubit can be minimized as the controllability is retained, realizing a modular architecture where the qubit and oscillator can be more independently optimized. This is important in applications where these spurious couplings can cause decoherence and distortion of encoded states, especially during idling periods[57]. Also, the approach could allow for the control of oscillators with measured relaxation times on the order of seconds[58] without reducing their lifetimes from the coupling to a lossy qubit through the Purcell effect[5].

Online content

Any methods, additional references, Nature Research reporting summaries, source data, extended data, supplementary information, acknowledgements, peer review information; details of author contributions and competing interests; and statements of data and code availability are available at https://doi.org/10.1038/s41567-022-01776-9.

References

1. Zurek, W. H. Decoherence, einselection, and the quantum origins of the classical. *Rev. Mod. Phys.* **75**, 715–775 (2003).
2. Haroche, S. Nobel lecture: controlling photons in a box and exploring the quantum to classical boundary. *Rev. Mod. Phys.* **85**, 1083–1102 (2013).
3. Chu, Y. et al. Quantum acoustics with superconducting qubits. *Science* **358**, 199–202 (2017).
4. Burkard, G., Gullans, M. J., Mi, X. & Petta, J. R. Superconductor–semiconductor hybrid-circuit quantum electrodynamics. *Nat. Rev. Phys.* **2**, 129–140 (2020).
5. Blais, A., Grimsmo, A. L., Girvin, S. M. & Wallraff, A. Circuit quantum electrodynamics. *Rev. Mod. Phys.* **93**, 025005 (2021).
6. Satzinger, K. J. et al. Quantum control of surface acoustic-wave phonons. *Nature* **563**, 661–665 (2018).
7. Arrangoiz-Arriola, P. et al. Resolving the energy levels of a nanomechanical oscillator. *Nature* **571**, 537–540 (2019).
8. Koolstra, G., Yang, G. & Schuster, D. I. Coupling a single electron on superfluid helium to a superconducting resonator. *Nat. Commun.* **10**, 5323 (2019).
9. Cortiñas, R. et al. Laser trapping of circular rydberg atoms. *Phys. Rev. Lett.* **124**, 123201 (2020).
10. Chakram, S. et al. Seamless high-Q microwave cavities for multimode circuit quantum electrodynamics. *Phys. Rev. Lett.* **127**, 107701 (2021).
11. Leghtas, Z. et al. Deterministic protocol for mapping a qubit to coherent state superpositions in a cavity. *Phys. Rev. A* **87**, 042315 (2013).
12. Krastanov, S. et al. Universal control of an oscillator with dispersive coupling to a qubit. *Phys. Rev. A* **92**, 040303 (2015).
13. Heeres, R. W. et al. Cavity state manipulation using photon-number selective phase gates. *Phys. Rev. Lett.* **115**, 137002 (2015).
14. Fösel, T., Krastanov, S., Marquardt, F. & Jiang, L. Efficient cavity control with SNAP gates. Preprint at https://arxiv.org/abs/2004.14256 (2020).

15. Kudra, M. et al. Robust preparation of Wigner-negative states with optimized SNAP-displacement sequences. *PRX Quantum* **3**, 030301 (2022).

16. Wang, W. et al. Converting quasiclassical states into arbitrary Fock state superpositions in a superconducting circuit. *Phys. Rev. Lett.* **118**, 223604 (2017).

17. Khaneja, N., Reiss, T., Kehlet, C., Schulte-Herbrüggen, T. & Glaser, S. J. Optimal control of coupled spin dynamics: design of NMR pulse sequences by gradient ascent algorithms. *J. Magn. Reson.* **172**, 296–305 (2005).

18. Heeres, R. W. et al. Implementing a universal gate set on a logical qubit encoded in an oscillator. *Nat. Commun.* **8**, 94 (2017).

19. Reinhold, P. *Controlling Error-Correctable Bosonic Qubits*. PhD thesis, Yale Univ. (2019).

20. Ma, W.-L. et al. Quantum control of bosonic modes with superconducting circuits. *Sci. Bull.* **66**, 1789–1805 (2021).

21. Roy, A. & Devoret, M. Introduction to parametric amplification of quantum signals with Josephson circuits. *C. R. Phys.* **17**, 740–755 (2016).

22. Aspelmeyer, M., Kippenberg, T. J. & Marquardt, F. Cavity optomechanics. *Rev. Mod. Phys.* **86**, 1391–1452 (2014).

23. Murch, K. W. et al. Cavity-assisted quantum bath engineering. *Phys. Rev. Lett.* **109**, 183602 (2012).

24. Pechal, M. et al. Microwave-controlled generation of shaped single photons in circuit quantum electrodynamics. *Phys. Rev. X* **4**, 041010 (2014).

25. Eddins, A. et al. Stroboscopic qubit measurement with squeezed illumination. *Phys. Rev. Lett.* **120**, 040505 (2018).

26. Rosenblum, S. et al. A CNOT gate between multiphoton qubits encoded in two cavities. *Nat. Commun.* **9**, 652 (2018).

27. Rosenblum, S. et al. Fault-tolerant detection of a quantum error. *Science* **361**, 266–270 (2018).

28. Touzard, S. et al. Gated conditional displacement readout of superconducting qubits. *Phys. Rev. Lett.* **122**, 080502 (2019).

29. Campagne-Ibarcq, P. et al. Quantum error correction of a qubit encoded in grid states of an oscillator. *Nature* **584**, 368–372 (2020).

30. Elder, S. S. et al. High-fidelity measurement of qubits encoded in multilevel superconducting circuits. *Phys. Rev. X* **10**, 011001 (2020).

31. Vrajitoarea, A., Huang, Z., Groszkowski, P., Koch, J. & Houck, A. A. Quantum control of an oscillator using a stimulated Josephson nonlinearity. *Nat. Phys.* **16**, 211–217 (2020).

32. Reagor, M. et al. Quantum memory with millisecond coherence in circuit QED. *Phys. Rev. B* **94**, 014506 (2016).

33. Flühmann, C. & Home, J. P. Direct characteristic-function tomography of quantum states of the trapped-ion motional oscillator. *Phys. Rev. Lett.* **125**, 043602 (2020).

34. Flühmann, C. et al. Encoding a qubit in a trapped-ion mechanical oscillator. *Nature* **566**, 513–517 (2019).

35. Sivak, V. V. et al. Model-free quantum control with reinforcement learning. *Phys. Rev. X* **12**, 011059 (2022).

36. Baum, Y. et al. Experimental deep reinforcement learning for error-robust gate-set design on a superconducting quantum computer. *PRX Quantum* **2**, 040324 (2021).

37. Niepce, D., Burnett, J. J., Kudra, M., Cole, J. H. & Bylander, J. Stability of superconducting resonators: motional narrowing and the role of Landau-Zener driving of two-level defects. *Sci. Adv.* **7**, eabh0462 (2021).

38. Backes, K. M. et al. A quantum enhanced search for dark matter axions. *Nature* **590**, 238–242 (2021).

39. Dassonneville, R. et al. Dissipative stabilization of squeezing beyond 3 dB in a microwave mode. *PRX Quantum* **2**, 020323 (2021).

40. Hastrup, J., Park, K., Filip, R. & Andersen, U. L. Unconditional preparation of squeezed vacuum from Rabi interactions. *Phys. Rev. Lett.* **126**, 153602 (2021).

41. Duivenvoorden, K., Terhal, B. M. & Weigand, D. Single-mode displacement sensor. *Phys. Rev. A* **95**, 012305 (2017).

42. Michael, M. H. et al. New class of quantum error-correcting codes for a bosonic mode. *Phys. Rev. X* **6**, 031006 (2016).

43. Gottesman, D., Kitaev, A. & Preskill, J. Encoding a qubit in an oscillator. *Phys. Rev. A* **64**, 012310 (2001).

44. Noh, K., Albert, V. V. & Jiang, L. Quantum capacity bounds of Gaussian thermal loss channels and achievable rates with Gottesman-Kitaev-Preskill codes. *IEEE Trans. Inf. Theory* **65**, 2563–2582 (2019).

45. Royer, B., Singh, S. & Girvin, S. M. Stabilization of finite-energy Gottesman-Kitaev-Preskill states. *Phys. Rev. Lett.* **125**, 260509 (2020).

46. Axline, C. J. et al. On-demand quantum state transfer and entanglement between remote microwave cavity memories. *Nat. Phys.* **14**, 705–710 (2018).

47. Hu, L. et al. Quantum error correction and universal gate set operation on a binomial bosonic logical qubit. *Nat. Phys.* **15**, 503–508 (2019).

48. Gertler, J. M. et al. Protecting a bosonic qubit with autonomous quantum error correction. *Nature* **590**, 243–248 (2021).

49. Burkhart, L. D. et al. Error-detected state transfer and entanglement in a superconducting quantum network. *PRX Quantum* **2**, 030321 (2021).

50. Hastrup, J., Park, K., Brask, J. B., Filip, R. & Andersen, U. L. Measurement-free preparation of grid states. *npj Quantum Inf.* **7**, 17 (2021).

51. de Neeve, B., Nguyen, T.-L., Behrle, T. & Home, J. P. Error correction of a logical grid state qubit by dissipative pumping. *Nat. Phys.* **18**, 296–300 (2022).

52. Grimsmo, A. L. & Puri, S. Quantum error correction with the Gottesman-Kitaev-Preskill code. *PRX Quantum* **2**, 020101 (2021).

53. Vuillot, C., Asasi, H., Wang, Y., Pryadko, L. P. & Terhal, B. M. Quantum error correction with the toric Gottesman-Kitaev-Preskill code. *Phys. Rev. A* **99**, 032344 (2019).

54. Noh, K., Chamberland, C. & Brandão, F. G. Low-overhead fault-tolerant quantum error correction with the surface-GKP code. *PRX Quantum* **3**, 010315 (2022).

55. Lingenfelter, A., Roberts, D. & Clerk, A. A. Unconditional Fock state generation using arbitrarily weak photonic nonlinearities. *Sci. Adv.* **7**, eabj1916 (2021).

56. Haljan, P. C., Brickman, K.-A., Deslauriers, L., Lee, P. J. & Monroe, C. Spin-dependent forces on trapped ions for phase-stable quantum gates and entangled states of spin and motion. *Phys. Rev. Lett.* **94**, 153602 (2005).

57. Albert, V. V. et al. Performance and structure of single-mode bosonic codes. *Phys. Rev. A* **97**, 032346 (2018).

58. Romanenko, A. et al. Three-dimensional superconducting resonators at $T < 20$ mK with photon lifetimes up to $\tau = 2$ s. *Phys. Rev. Appl.* **13**, 034032 (2020).

Methods

Oscillator relaxation and dephasing in displaced frame

With photon loss at rate κ, the oscillator's density matrix evolves according to the quantum master equation in the Lindblad form as

$$\partial_t \rho = -i[H, \rho] + \kappa \mathcal{D}[a]\rho, \tag{2}$$

$$H = H_0 + \varepsilon a^\dagger + \varepsilon^* a, \tag{3}$$

where $\mathcal{D}[L] = L\rho L^\dagger - (1/2)\{L^\dagger L, \rho\}$ and H_0 is the oscillator's Hamiltonian; we have included a time-dependent oscillator drive $\varepsilon(t)$. Here we take $\hbar = 1$. The evolution of the density matrix in a time-dependent displaced frame $\tilde{\rho} = D^\dagger(\alpha)\rho D(\alpha)$ is given by the equivalent master equation:

$$\partial_t \tilde{\rho} = -i[\tilde{H}, \tilde{\rho}] + \kappa \mathcal{D}[a + \alpha]\tilde{\rho}, \tag{4}$$

$$\tilde{H} = D^\dagger(\alpha) H_0 D(\alpha) + (-i\partial_t \alpha + \varepsilon)a^\dagger + \text{h.c.} \tag{5}$$

In particular, the displaced-frame Lindbladian can be recast as

$$\kappa \mathcal{D}[a + \alpha]\tilde{\rho} = \kappa \mathcal{D}[a]\tilde{\rho} - i\left[i\frac{\kappa}{2}(\alpha^* a - \alpha a^\dagger), \tilde{\rho}\right], \tag{6}$$

corresponding to photon loss at rate κ and a Hermitian re-centring force at rate $\frac{\kappa}{2}|\alpha|$. This deterministic force can be lumped into the effective displaced-frame Hamiltonian, giving

$$\partial_t \tilde{\rho} = -i[\tilde{H}, \tilde{\rho}] + \kappa \mathcal{D}[a]\tilde{\rho}, \tag{7}$$

$$\tilde{H} = D^\dagger(\alpha) H_0 D(\alpha) + \left(-i\partial_t \alpha - i\frac{\kappa}{2}\alpha + \varepsilon\right)a^\dagger + \text{h.c.} \tag{8}$$

Given a desired $\alpha(t)$, $\varepsilon(t)$ can be chosen such that the term in the parentheses is zero, satisfying the classical Langevin equation for $\alpha(t)$ given in the main text and counteracting the re-centring force. With this choice of drive, the deterministic evolution is accounted for, and relaxation in the displaced frame is not enhanced compared with relaxation at the origin of the phase space. The classical drive equation can also be modified to account for all the linear terms in $\tilde{H}$, including those caused by nonlinear terms in H_0 (Supplementary Section 4).

White-noise oscillator dephasing is given by the master equation $\partial_t \rho = 2\kappa_\phi \mathcal{D}[a^\dagger a]\rho$. Defining the superoperator $\mathcal{S}[X, Y]\rho = X\rho Y^\dagger - \{Y^\dagger X, \rho\}$ oscillator dephasing is transformed in the displaced frame to

$$\begin{aligned}
\partial_t \tilde{\rho} &= 2\kappa_\phi \mathcal{D}[(a^\dagger + \alpha^*)(a + \alpha)]\tilde{\rho} \\
&= 2\kappa_\phi \{\mathcal{D}[a^\dagger a]\tilde{\rho} + |\alpha|^2(\mathcal{D}[a]\tilde{\rho} + \mathcal{D}[a^\dagger]\tilde{\rho}) \\
&\quad + \alpha^2 \mathcal{S}[a^\dagger, a]\tilde{\rho} + \alpha^{*2}\mathcal{S}[a, a^\dagger]\tilde{\rho} \\
&\quad + \alpha(\mathcal{S}[a^\dagger a, a]\tilde{\rho} + \mathcal{S}[a^\dagger, a^\dagger a]\tilde{\rho}) \\
&\quad + \alpha^*(\mathcal{S}[a^\dagger a, a^\dagger]\tilde{\rho} + \mathcal{S}[a, a^\dagger a]\tilde{\rho})\}.
\end{aligned} \tag{9}$$

In the displaced frame, the noise is dominated by diffusion-like terms at rate $2\kappa_\phi|\alpha|^2$; unlike the relaxation case, there is no deterministic part that can be counteracted with a simple displacement. However, this master equation is only valid in the Markovian regime; typically, the spectral density of the oscillator frequency fluctuations are due to non-white effects such as two-level-system defects[37]. In the case of coloured noise, it is possible that part of the enhanced dephasing noise could be echoed away using symmetric pulse constructions[59].

Universality of ECD control

The universal control of the oscillator is the ability to perform arbitrary unitary transformations that are generated by Hamiltonians polynomial in $q = (1/\sqrt{2})(a^\dagger + a)$ and $p = (i/\sqrt{2})(a^\dagger - a)$ (refs. [60,61]). Here we extend this definition to the universal control of the oscillator and qubit, which is the ability to perform arbitrary unitary transformations that are generated by linear combinations of Hamiltonians of the form $q^j p^k \sigma_i$, where j, k are non-negative integers and $\sigma_i \in \{I, \sigma_x, \sigma_y, \sigma_z\}$.

Given a set of generating Hamiltonians $\{A, B\}$, the two identities, namely,

$$e^{-iA\delta t}e^{-iB\delta t}e^{iA\delta t}e^{iB\delta t} = e^{[A,B]\delta t^2} + O(\delta t^3), \tag{10}$$

$$e^{iA\delta t/2}e^{iB\delta t/2}e^{iB\delta t/2}e^{iA\delta t} = e^{i(A+B)\delta t} + O(\delta t^3), \tag{11}$$

can be used to generate the action of the Hamiltonian $-i[A, B]$ and the Hamiltonian $A + B$ in the limit $\delta t \to 0$ (ref. [61]). By the repeated application of the identities above, we can generate the evolution that is any superposition of the nested commutators of the original set of generators[62].

Starting with the set of generators for ECD(β) and $R_\varphi(\theta)$, namely, $\{q\sigma_z, p\sigma_z, \sigma_x, \sigma_y\}$, commutators such as $[q\sigma_z, \sigma_x] \propto q\sigma_y$ and $[\sigma_x, \sigma_y] \propto \sigma_z$ can be used to expand the set to $\{\sigma_i, q\sigma_i, p\sigma_i\}$, where $i \in \{x, y, z\}$. This effectively shows that by rotating the qubit between conditional displacements, the ECD gate set can create more general Rabi-type interactions between the oscillator and qubit, where qubit-mediated nonlinear gates have been proposed[63,64].

By using commutators similar to $[q\sigma_x, q\sigma_y] \propto q^2\sigma_z$, our set can be further expanded to all the quadratic polynomials of $q\sigma_i$ and $p\sigma_i$. This process can be iterated to generate any $q^j p^k \sigma_i$ product, where $i \in \{x, y, z\}$. Terms that do not contain a Pauli operator such as $q^j p^k$ can be generated from commutators such as $[q^{j+1}p^k\sigma_z, p\sigma_z] \propto q^j p^k$. With this, the full Lie algebra for polynomial operators on the qubit and oscillator Hilbert space is generated.

Speed limit of control

The maximum interaction rate between the oscillator and qubit will be limited by the maximum displacement in the oscillator before higher-order nonlinear effects begin to invalidate the dispersive approximation. From another work[5], the critical oscillator photon number for the jth transmon state is

$$n_{\text{crit}}^j = \frac{1}{2j+1}\left(\frac{|\Delta - jE_C|^2}{4g^2} - j\right), \tag{12}$$

where Δ is the transmon–oscillator detuning, g is the linear transmon–oscillator coupling rate and E_C is the charging energy of the transmon. For our experimental parameters, $n_{\text{crit}}^g \approx 2,740$ and $n_{\text{crit}}^e \approx 910$. These bounds are not strict; however, they provide a guiding principle for the maximum photon number before higher-order effects become important (Supplementary Section 3).

With this, the maximum conditional displacement rate is $g_{\text{eff}}^{\text{max}} = \alpha_0^{\text{max}}\chi \approx \sqrt{n_{\text{crit}}^e}\chi$ using the critical photon number for the first excited state of the transmon. From perturbation theory, the transmon–oscillator dispersive coupling is $\chi \approx (2g^2 E_C)/(\Delta(\Delta - E_C))$ and the transmon anharmonicity is $K \approx E_C$ (ref. [5]). In the regime $\Delta \gg E_C$, we can approximate $\Delta - E_C \approx \Delta$ and combine the above expressions to find

$$g_{\text{eff}}^{\text{max}} \approx \sqrt{\frac{\chi K}{6}}. \tag{13}$$

We note that other experiments using sideband three-wave-mixing interactions are similarly limited by a bound directly proportional to $\sqrt{\chi K}$ (refs. [24,26,28]). This suggests that at a fixed dispersive shift, increasing the transmon anharmonicity could lead to faster interaction rates,

giving a path forward for engineering higher-fidelity gates with enhanced effective three-wave interactions.

Data availability
The data that support the findings of this study are available from the corresponding authors upon reasonable request.

Code availability
The code used for gate and pulse optimization is available via GitHub at https://github.com/alec-eickbusch/ECD_control.

References
59. Ball, H. et al. Software tools for quantum control: improving quantum computer performance through noise and error suppression. *Quantum Sci. Technol.* **6**, 044011 (2021).
60. Lloyd, S. & Braunstein, S. L. Quantum computation over continuous variables. *Phys. Rev. Lett.* **82**, 1784–1787 (1999).
61. Braunstein, S. L. & van Loock, P. Quantum information with continuous variables. *Rev. Mod. Phys.* **77**, 513–577 (2005).
62. D'Alessandro, D. *Introduction to Quantum Control and Dynamics* (CRC Press, 2007).
63. Park, K., Marek, P. & Filip, R. Qubit-mediated deterministic nonlinear gates for quantum oscillators. *Sci. Rep.* **7**, 11536 (2017).
64. Park, K., Marek, P. & Filip, R. Deterministic nonlinear phase gates induced by a single qubit. *New J. Phys.* **20**, 053022 (2018).

Acknowledgements

Author contributions
A.E., S.S.E., M.H.D. and R.J.S. developed the large displacement control method. A.E., S.R.J., V.S. and A.Z.D. implemented the numerical ECD parameter optimization. A.E., V.S. and A.Z.D. conducted the measurements. A.E., B.R., V.S. and S.M.G. developed the theory. J.V. and A.E. performed the numerical analysis of the strongly driven nonlinear oscillator. A.E. and M.H.D. wrote the manuscript with feedback from all the authors.

Competing interests
R.J.S. and M.H.D. are founders and R.J.S. is a shareholder of Quantum Circuits. The remaining authors declare no competing interests.

Additional information